Journal of Water Resource and Protection, 2019, 11, 357-370
http://www.scirp.org/journal/jwarp
ISSN Online: 1945-3108
ISSN Print: 1945-3094

Comparative Study on the Effects of Surface Area, Conduction Band and Valence Band Positions on the Photocatalytic Activity of ZnO-M_xO_y Heterostructures

Mysore Byrappa Nayan[1], Krishnegowda Jagadish[1], Mavinakere Ramesh Abhilash[1], Keerthiraj Namratha[2,3], Shivanna Srikantaswamy[1*]

[1]Department of Studies in Environmental Science, University of Mysore, Mysuru, India
[2]Center for Materials Science and Technology, Vijnana Bhavana, University of Mysuru, Mysuru, India
[3]Department of Studies in Earth Science, University of Mysore, Mysuru, India

Email: *srikantas@hotmail.com

How to cite this paper: Nayan, M.B., Jagadish, K., Abhilash, M.R., Namratha, K. and Srikantaswamy, S. (2019) Comparative Study on the Effects of Surface Area, Conduction Band and Valence Band Positions on the Photocatalytic Activity of ZnO-M_xO_y Heterostructures. *Journal of Water Resource and Protection*, **11**, 357-370.
https://doi.org/10.4236/jwarp.2019.113021

Received: February 6, 2019
Accepted: March 25, 2019
Published: March 28, 2019

Abstract

ZnO-M_xO_y heterostructures (M=Co, Mn, Ni, or In) are fabricated via hydrothermal synthesis method. X-ray diffraction and Fourier-transform infrared spectroscopy analyses endorse the successive formation of the various heterostructures. Field Emission Scanning electron microscope and Brunauer-Emmett-Teller (BET) surface area studies confirm the porous nature of the heterostructures obtained. The band gaps of various heterostructures are calculated that, 3.1, 2.71, 2.64, and 2.19 eV for ZnO-NiO, ZnO-In_2O_3, ZnO-Co_3O_4, and ZnO-MnO_2, respectively. The photocatalytic activities of the fabricated heterostructures are investigated through the degradation of phenol under direct sunlight irradiation. The results show that the photocatalytic activity is affected by the conduction band (CB) and valence band (VB) positions rather than surface area of ZnO-M_xO_y heterostructure nanocomposites.

Keywords

Metal Oxide Heterostructures, ZnO-M_xO_y Nanocomposites, Hydrothermal Synthesis, Solar-Driven Photocatalysis, Phenol Degradation

1. Introduction

Water pollution has become one of the serious problems that threaten human life. Photocatalytic degradation is a promising green technology to remove organic and inorganic pollutants from the water. A lot of metal oxide semicon-

ductors have been explored for photocatalytic pollutant degradation [1] [2]. Zinc oxide (ZnO) semiconductor is extensively used as a photocatalyst in the photodegradation of organic and inorganic pollutants [3]. However, there are several drawbacks linked with the higher rates of charge carrier and recombination, and this can only absorb a small percentage of the solar light in the UV region owing to the wide band gap [4]. Hence, it restricts photocatalytic applications under the visible-light illumination [5] and it has posed a challenge to researchers for the effective utilization in the photocatalytic applications. In order to overcome these limitations, researchers did many attempts to tailor the band gap of ZnO including intrinsic [6] [7] and extrinsic [8] [9] doping and coupling ZnO with other semiconductor systems. It is well-known that the introductions of extrinsic or intrinsic defects, which cause defect related states in the form of band tail, promote the extension of photonic absorption to the broader visible region or band gap narrowing. Coupling ZnO with other narrow band gap semiconductors like CuO, Fe_2O_3, WO_3, CdS, ZnS, etc. can reduce the band gap and extend the light absorption range of ZnO to a broader spectrum of the visible light, and promote electron-hole pair separation under sunlight irradiation in order to achieve higher photocatalytic activity [10]. The present authors have worked on coupled ZnO with CeO_2 and Bi_2O_3 to construct Bi_2O_3-CeO_2-ZnO heterostructure [11]. Bi_2O_3-CeO_2-ZnO exhibited improved photocatalytic activity due to the extended visible-light photoabsorption range benefited from the presence of Bi_2O_3 (small band gap of 2.77 eV) and efficient separation of photo-induced electrons and holes caused by the vector transfer of electrons and holes among ZnO, CeO_2 and Bi_2O_3 [11]. On the other hand, usually the photocatalytic activity of a photocatalyst is strongly influenced by its surface area. The higher surface area, the higher number of active photocatalytic sites, the higher adsorption capability for the pollutants on the photocatalyst surface, and the higher photocatalytic activity [12] [13] [14]. Although there are several methods available to process these metal oxides, but hydrothermal technique is becoming very popular in recent years, because of its environmentally benign and facilitates *in situ* surface modification, which provides fabrication of nanoparticles with desired tailor-made properties [15] [16] [17] [18]. In the present work, an attempt has been made to understand a unique comparative study on the effects of surface area, CB and VB positions and band gap of ZnO based metal oxide (ZnO/M_xO_y) heterostructures for their photocatalytic activities, whereas ZnO/M_xO_y are ZnO/MnO_2, ZnO/Co_3O_4, ZnO/NiO and ZnO/In_2O_3. The photocatalytic efficiency of these coupled semiconductor systems have been tested by monitoring phenol degradation under solar irradiation.

2. Experimental Details

2.1. Materials

The ingredients were procured through different commercial suppliers as follows: $Zn(NO_3)_2 \cdot 6H_2O$ (Alfa Aesar, 99%), $Ni(NO_3)_2 \cdot 6H_2O$ (Sigma Aldrich, 99.99%, $Co(NO_3)_2 \cdot 6H_2O$ (Loba Chemie, 99.8%), $In(NO_3) \cdot xH_2O$ (Sigma-Aldrich, 99.99%),

$Mn(NO_3)\cdot 4H_2O$ (Alfa Aesar, 98%) and NaOH (Sigma-Aldrich, 97%). Ultra-pure water (18. 2 MΩ·cm) was used in the experiments.

2.2. Hydrothermal Synthesis of ZnO/M_xO_y Nanocomposite

The synthesis of ZnO/M_xO_y nanocomposites were carried out by using 15 ml 0.1M $Zn(NO_3)_2\cdot 6H_2O$ mixed with 15 ml 0.1M along with a desired metal nitrate ($Ni(NO_3)_2\cdot 6H_2O$, $Co(NO_3)_2\cdot 6H_2O$, $Mn(NO_3)_2\cdot 4H_2O$ or $In(NO_3)\cdot xH_2O$). The mixed solution was ultrasonicated thoroughly and mixed for 30 minutes to get the homogenous mixture. Later, about 24 ml of the suspension was transferred into a 30 ml capacity Teflon liner and closed tightly. The percent fill was kept at 80% in all experiments. The Teflon liner was inserted into SS316 Stainless Steel autoclave and heated up to a particular temperature for a required period of time (Table 1). The autoclave was cooled down to the laboratory temperature after hydrothermal reaction and the resultant material in the Teflon liner was filtered and washed with distilled water and ethanol. Later, the product obtained was dried at around 80˚C in a hot air oven for 12 hours. Table 1 gives the experimental hydrothermal conditions used in the synthesis of $ZnO\text{-}M_xO_y$ heterostructure nanocomposites.

2.3. Characterization

The prepared heterostructures were characterized using Rigaku Smart Lab-II X-ray diffractometer (XRD) with CuKα radiation (λ = 1.540598 Å), Carl Zeiss MERLIN Compact field emission scanning electron microscopy (FE-SEM), JASCO 460 plus FTIR spectrometer, a Shimadzu UV-2450 spectrophotometer (UV-Vis DRS), NETZSCH, Germany, Model STA 2500 Regulus, thermo-gravimetric analysis (TGA), and BELSORP MINI 2, BEL, Japan, Brunauer-Emmett-Teller (BET) surface area measurements.

2.4. Photocatalytic Test

The photocatalytic properties of as synthesized $ZnO\text{-}M_xO_y$ nanocomposites were carried out for the study of phenol degradation. The degradation was performed under solar light irradiation to the phenol sample with the catalyst $ZnO\text{-}M_xO_y$ nanocomposites. The phenol samples with different concentrations, like 8, 16, 24 and 32 ppm, were prepared and the optimum phenol degradation concentration was investigated for the different catalysts. In typical procedure, the degradation

Table 1. Experimental conditions used in the fabrication of M_xO_y nanocomposites.

ZnO/M_xO_y composite	Ratio	Temperature (˚C)	Hydrothermal reaction time duration (hr)
ZnO/MnO_2	1:1	180	5
ZnO/NiO	1:1	160	5
ZnO/Co_3O_4	1:1	150	6
ZnO/In_2O_3	1:1	180	8

was carried out by preparing 100 ml of phenol solution with above mentioned different concentration in a 250 cm^3 conical flasks. Later, 0.5 g of the catalysts such as ZnO-M_xO_y nanocomposites were added to individual flasks and closed tightly with rubber cork. The degradation reaction was carried out for the period of 3 h (from 11 am to 2 am in a sunny day in April 2018 in Mysuru, India) under solar light irradiation. After the completion of degradation reaction, the samples were filtered and the percentage of phenol degradation was investigated by performing chemical oxygen demand (COD) analysis.

3. Results and Discussion

3.1. The Powder XRD Analysis

Figure 1 shows the powder XRD patterns of pure ZnO and heterogeneous semiconductor ZnO-M_xO_y nanocomposites. It is clear indicates that, all the diffraction peaks of ZnO can be indexed to the hexagonal wurtzite structure according to JCPDS card N (JCPDS: 36-1451) [19] and peaks corresponds to heterostructured composites consist of different phases. The XRD pattern of heterostructured ZnO-Co_3O_4 composite indicates that it consists of two kinds of phases, hexagonal ZnO and spinel structured cubic Co_3O_4 (JCPDS card # 43-1003) confirming the coexistence of Zn and Co oxide structure together to form a composite however, the peaks of Co_3O_4 are weak compared with ZnO and it is matched with the data reported by Zhang *et al.* [20]. The XRD pattern of heterostructured ZnO-NiO composite indicates that it consists of two phases, hexagonal ZnO and cubic structured rocksalt type NiO phase (JCPDS-78-0643) showing the coexistence of Zn and Ni oxide structures together to form heterogeneous composite. The XRD pattern of heterostructured ZnO-MnO_2 composite specifies that it consists of two kind of phases, hexagonal ZnO and birnessite δ-MnO_2 crystal phase (JCPDS 80-1098) [21] which indicates that the coexistence of Zn and Mn oxide structures together to form heterogeneous heterostructure

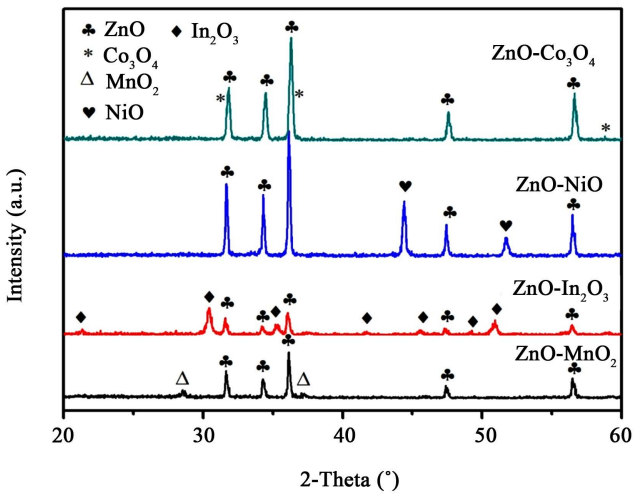

Figure 1. Powder X-ray diffraction patterns characteristic samples of ZnO-M_xO_y nanocomposites.

composite [22]. The powder XRD pattern of heterostructured ZnO-In_2O_3 composite postulates that it consists of two kind of phases, hexagonal ZnO and bixbyite type In_2O_3 of cubic system crystal phase indicates that the coexistence of Zn and In oxide structures together to form heterogeneous composite. The XRD pattern of ZnO-In_2O_3 is in agreement with the earlier reported pattern [23]. The intensity of standard ZnO decreased in all heterogeneous composites, due to the major reflections of other metal oxides which were entrapped in intense ZnO reflections. This mechanism leads to the growth of heterogeneous composites with different crystal phases. The powder patterns show well crystallized metal oxides with a higher degree of crystallinity forming M_xO_y nanocomposites.

3.2. FTIR Analysis

The FTIR analysis of heterostructured ZnO-M_xO_y nanocomposites was performed. Figure 2 shows the FTIR spectra and the bands are observed near 3445 cm^{-1} and 1630 cm^{-1} correspond to the O-H stretching and bending vibration of water molecules adsorbed on the surface of nanocomposites due to the porosity as noticed in the images of electron microscopic study.

The carbonate peaks are prominent in all the composites and it is again attributed to the absorption of CO_2 from the atmosphere. The finger print region of metal oxygen bond shows the characteristic absorption bands in the wavenumber region 400 to 600 cm^{-1} [11]. This finger print range shows the metal oxygen bond presence of different metal oxygen of ZnO-M_xO_y nanocomposites. Usually ZnO shows flower like, or interlocked rod like structure, and other metal oxides like CO_3O_4 , In_2O_3, NiO, and MnO_2, show a different morphology (either tabular, or massive rounded to sub-rounded). The bonding of composites have metal and oxygen bond between Zn-O, Ni-O, Mn-O, In-O and Co-O along with the absorption peak at wavenumber range 1402 - 1506 cm^{-1} indicates the presence of CO_2, which was due to the atmospheric CO_2 interference during analysis [11] [19]. Apparently, the FTIR results further support the formation

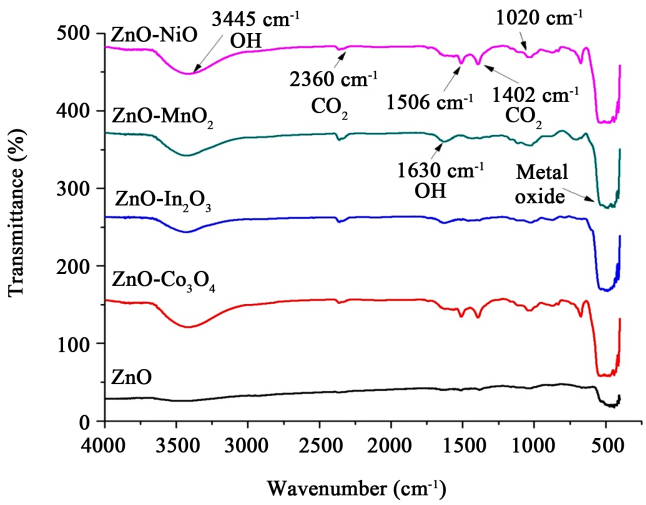

Figure 2. Characteristic FTIR spectra of ZnO-M_xO_y nanocomposites.

of the heterostructured nanocomposites and agree well with XRD results.

3.3. FESEM Analysis

Figure 3 shows FE-SEM images of ZnO-M_xO_y nanocomposites and it is observed that ZnO-Co_3O_4 and ZnO-In_2O_3 show fine interlocked nanorods showing porous structure, whereas ZnO-NiO and ZnO-MnO_2 show still finer structures with smaller rods and also showing the interlocked porous structure. This is a very typical characteristic of ZnO-M_xO_y nanocomposites. It is further observed that the particles have narrow-size distribution. The average particle size distribution of ZnO-M_xO_y nanocomposites is shown in Figure 4. Among the nanocomposites synthesized, ZnO-In_2O_3 have highest particle size (140 nm) and ZnO-NiO have the least particle size (40 nm). This kind of interlocked structure shows higher porosity and in turn higher BET surface area. It is also evident from FTIR spectra that, ZnO-M_xO_y nanocomposites have the surface adsorption of CO_2 and O-H.

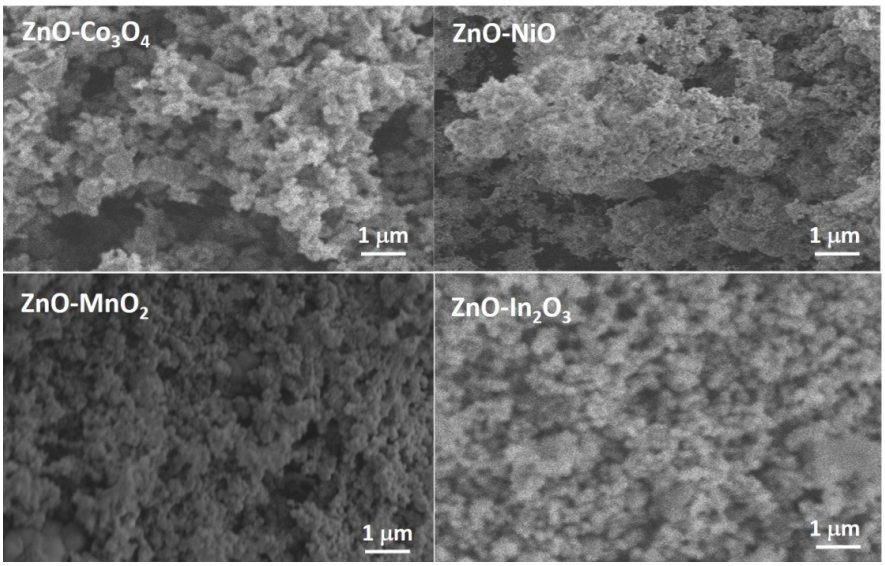

Figure 3. FESEM images of characteristic ZnO/M_xO_y nanocomposites.

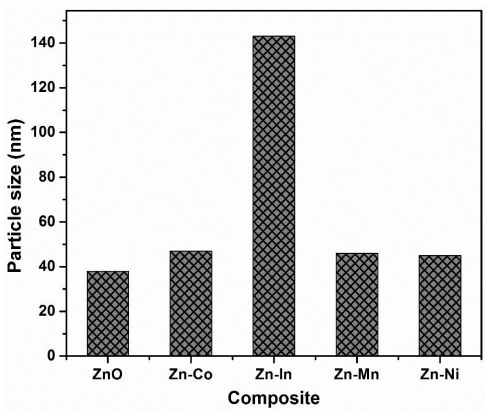

Figure 4. Particle size distribution of ZnO-M_xO_y nanocomposites.

3.4. DLS Analysis

Particle size distributions of as prepared nanocomposites are shown in **Figure 4**. The analysis was carried out by DLS instrument, in which the size measurement was based on the Brownian motion of particle in the solvent media. The results as evident from **Figure 4**, indicate that the average particle size (nm) of the nanocomposites prepared by hydrothermal reaction conditions. The average particle size of pure ZnO, composites ZnO-Co_3O_4, ZnO-In_2O_3, ZnO-MnO_2 and ZnO-NiO was 38, 47, 143, 46 and 44 respectively. The pure ZnO shows the lowest and composite ZnO-In_2O_3 shows highest average particle size. The results obtained from DLS corresponding with the results of FESEM images. It was described that the highest particle size from the composite ZnO-In_2O_3 due to the high atomic/ionic radius (167 pm) of Indium atom, when compared to the other metals from the composite. Further the composites, prepared from the hydrothermal reaction show the size within 100 nm range except ZnO-In_2O_3 and indicates that the confirmation of nanocomposite formation.

3.5. UV-Vis Spectroscopic Analysis

The DRS UV-Vis spectra of as-synthesized ZnO-M_xO_y nanocomposites were recorded to determine their light absorption characteristics and **Figure 5** shows the DRS UV-Vis spectra of heterostructured nanocomposites. ZnO-MnO_2 shows the highest visible light absorption while ZnO-NiO shows the lowest visible light absorption. The band gaps of the various heterostructures were obtained from Tauc plot displayed in **Figure 5(b)** [24] [25]. Obviously, the band gap of the four heterostructures followed the trend of ZnO-NiO (3.1 eV) > ZnO-In_2O_3 (2.71 eV) > ZnO-Co_3O_4 (2.64 eV) > ZnO-MnO_2 (2.19 eV).

3.6. TGA Analysis

The thermal analysis of as synthesized ZnO-M_xO_y nanocomposites was carried out to get information about change in composites properties as function of temperature. **Figure 6** shows the TGA curves obtained under inert nitrogen environment for the nanocomposites. TGA curve indicate that the change in weight loss (%). The TGA curve of ZnO-Co_3O_4 shown that, the gradual decrease

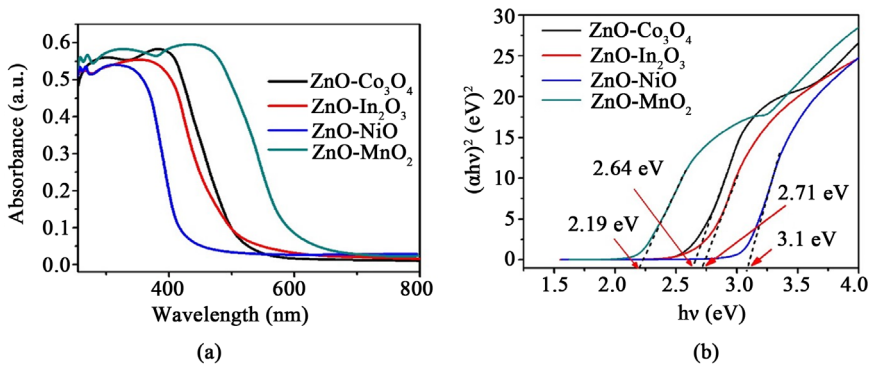

Figure 5. UV-Vis absorbance spectrum and Tauc plot of ZnO-M_xO_y nanocomposites.

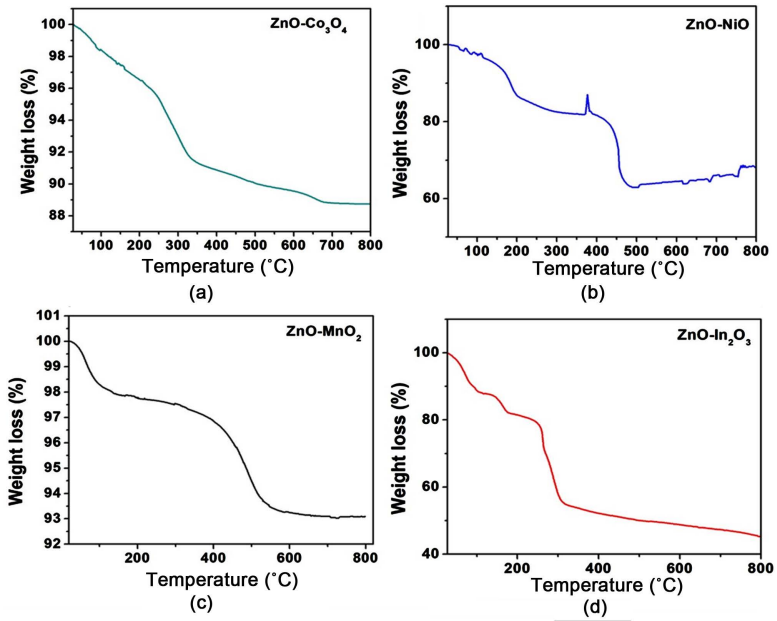

Figure 6. TGA curves of ZnO-M_xO_y nanocomposites.

in the weight at 105˚C, attributed to the evaporation of any residual water. Further decrease in the weight loss up to 290˚C was due to the evaporation of CO_2. The presence of CO_2 was evident from the FTIR analysis as well as the sudden loss in the weight% at temperature 290˚C to 350˚C was due to the decomposition of Co_3O_4 which in turn form Co_3O_4 and O_2. The total weight loss of ZnO-Co_3O_4 was ~15% and it shows high thermal stability. TGA curve at the temperature range between 40˚C - 180˚C and 190˚C - 375˚C of ZnO-NiO composite shows the weight loss occurred due to evaporation of water and CO_2 respectively. Again the sudden increase in the weight at temperature range between 380˚C - 390˚C occurred due to the re-adsorption of CO_2 with the influence of fluid N_2. Further the sudden decrease in the weight loss at temperature between 440˚C - 520˚C was due to the decomposition of composites. The TGA curve of ZnO-MnO_2 composite shows the curve with gradual decrease in the weight loss at temperature 40˚C - 150˚C due to evaporation of water molecules. Further the weight loss at temperature 420˚C - 550˚C was due to the thermal decomposition of ZnO-MnO_2 to MnO_2, and also the total weight loss observed was only ~8%, which depicts the higher thermal stability. The TGA of ZnO-In_2O_3 composite shows that the gradual decrease of weight loss at 40˚C - 120˚C and 150˚C - 240˚C indicate the evaporation of water and CO_2 respectively. Further the sudden decrease in the weight loss at 280˚C - 330˚C was due to the decomposition of composite, with a larger weight loss (35%).

3.7. BET Surface Area

The N_2 sorption isotherms of all samples can be classified as type IV with H_3 hysteresis loops (**Figure 7**), which means the existence of slit-like mesopores (2 - 50 nm) formed between aggregated nanoparticles [26]. The hysteresis loops of

all samples spanned a large P/P0 range (0.3 - 1.0), corresponding to the presence of mesopores. The surface area of the various samples follows the order: ZnO-MnO_2 (58.4 m^2/g) > ZnO-NiO (41.6 m^2/g) > ZnO-Co_3O_4 (39.6 m^2/g) > ZnO-In_2O_3 (22.7 m^2/g). In comparison with DLS results, the lowest surface area is shown by ZnO-In_2O_3 with the larger particle size. The pore size distribution of the samples (Figure 7) further confirms the formation of mesopores. As can be seen, the pore size distribution curve is quite broad (from 2 to 100 nm) with small and large mesopores (in the range of 2 - 50 nm). The small mesopores may reflect porosity within the nanoparticles and the large mesopores are associated to the pores formed between the nanoparticles [27].

3.8. Photocatalytic Properties of ZnO-M_xO_y Nanocomposites

The photocatalytic activities of the as prepared nanocomposites were performed by using phenol as a model organic pollutant in an aqueous solution for the degradation process. Figure 8 shows Chemical Oxygen Demand level of phenol

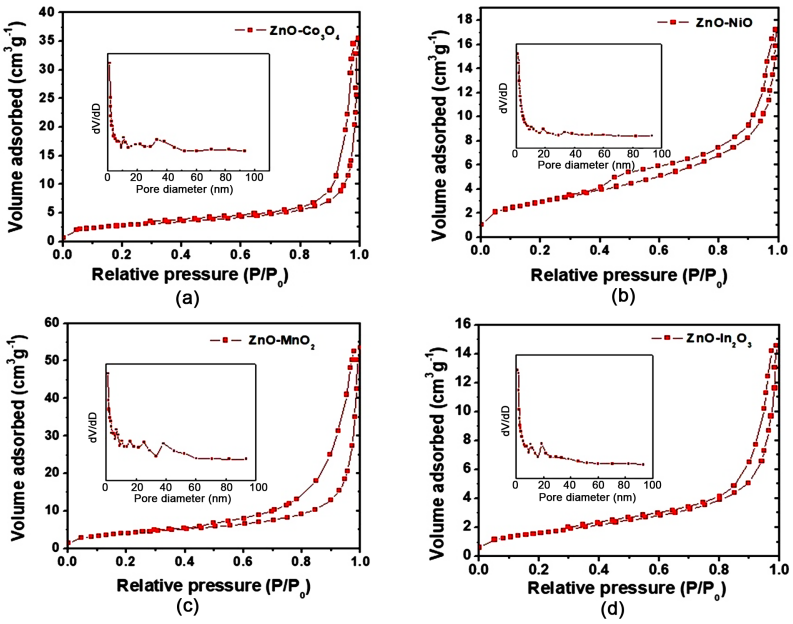

Figure 7. BET N_2 adsorption isotherm of ZnO-M_xO_y nanocomposites.

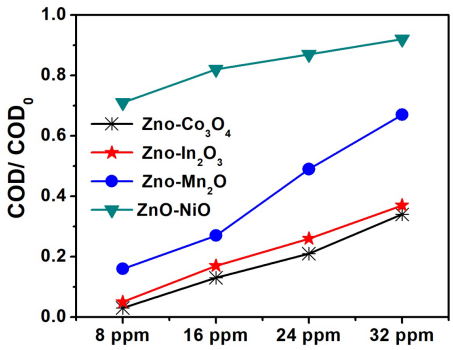

Figure 8. COD of ZnO-M_xO_y nanocomposites.

degradation in different concentrations of various composites under sunlight irradiation for the period of 3 hours. The order of phenol degradation follows the trends: ZnO-Co_3O_4 > ZnO-In_2O_3 > ZnO-MnO_2 > ZnO-NiO. Apparently, the order of phenol degradation does not follow the order of surface area, but it may occur because of the chemical composition of composites. The photocatalytic degradation was maximum by using ZnO-Co_3O_4, where 97% of 8 ppm of phenol have been degraded followed with 95% degradation by ZnO-In_2O_3, 84% degradation by ZnO-MnO_2 and 29% degradation by ZnO-NiO respectively. The degradation efficiency decreased when the concentration of phenol increased from 8 ppm to 32 ppm, which may be due to phenol molecules around the photocatalytic active sites resulted in inhibiting the penetration of light to the surface of the catalyst. Hence, the generation of relative amount of $^{\cdot}OH$ and $^{\cdot}O_2^-$ on the surface of the catalyst decreased [28]. The heterostructure catalysts were further tested for repetitive processes of photocatalytic degradation. It was found that the photocatalytic degradation efficiency did not decrease even after 3 cycles of photodegradation.

3.9. Plausible Mechanism of Phenol Degradation

The band gaps and band positions were calculated and the band structure diagrams of the different nanocomposites were presented in **Figure 9**, which is

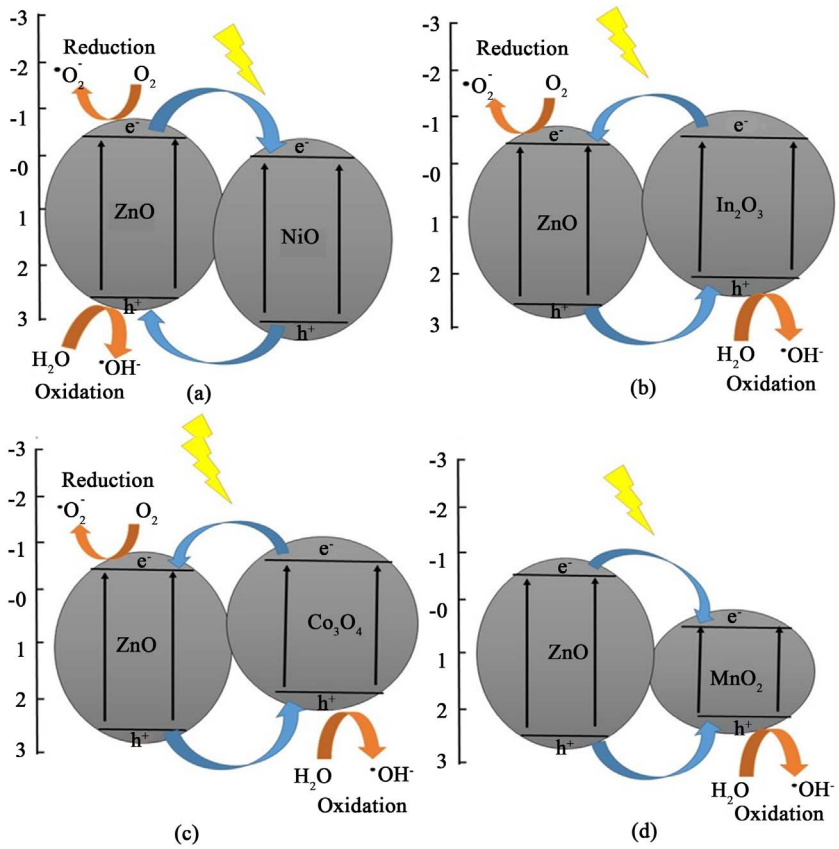

Figure 9. Photocatalysis mechanism of ZnO-M_xO_y nanocomposites.

helpful in understanding the mechanism of phenol degradation. The enhancement in the photocatalytic activity of ZnO-Co_3O_4 and ZnO-In_2O_3 can be attributed to the small band gap of ZnO-In_2O_3 (2.71 eV) and ZnO-Co_3O_4 (~2.64 eV) which results in improving the visible light absorption, and the enhancement in the charge separation occurs because of coupling ZnO with Co_3O_4 and In_2O_3 separately [29] [30] [31]. In case of Co_3O_4-ZnO nanocomposite, the electrons are accumulated in the conduction band (CB) of ZnO and the holes in the valance band (VB) of Co_3O_4 because the difference in the band edges positions. Similarly, in In_2O_3-ZnO nanocomposite, the electrons migrate to the CB of ZnO and the holes to the VB of In_2O_3 leading to inhibiting the electron hole recombination and enhancing the charge carrier separation efficiency and thus enhanced the photocatalytic activity. The electronic structure and band gap movement and also defect states have been studied in detail using XPS and photoluminescence spectroscopy. These results will be published elsewhere as a part of a detailed mechanism for heterostructure metal oxides nanocomposites.

Although the band gap of ZnO-MnO_2 (2.19 eV) is smaller than ZnO-In_2O_3, ZnO-Co_3O_4 and ZnO-NiO shows lower photocatalytic activity and the reason is charge separation efficiency of ZnO-MnO_2 is very low when compared with ZnO-Co_3O_4 and ZnO-In_2O_3. This process is indicated clearly in **Figure 9**, where the electrons and holes are accumulated in the CB and VB of MnO_2 which leads to high electron-hole recombination rate and thereby low photocatalytic activity. Moreover, the CB edge of MnO_2 is lower than the potential required to produce superoxide radicals ($^{\cdot}O_2^-$), hence only hydroxyl radicals ($^{\cdot}OH$) take part in the phenol degradation over ZnO-MnO_2 leading to further decrease in the photocatalytic activity [32]. The low photocatalytic activity of ZnO-NiO under sunlight irradiation due to the large band gap of ZnO-NiO (3.1 eV) leads to low light absorption and hence low photocatalytic activity occurred.

4. Conclusion

ZnO-Co_3O_4, ZnO-In_2O_3, ZnO-MnO_2, and ZnO-NiO heterostructures were fabricated via facile hydrothermal route. The successive formation of heterostructures and their purity were confirmed by XRD analysis. FT-IR analysis further verified that fabricated heterostructures are metal oxides and no other impurities. SEM and BET studies revealed that the heterostructures obtained exhibit porous nature. TGA analysis shows that the highest and lowest thermal stability were exhibited by ZnO-MnO_2 and ZnO-In_2O_3 respectively. The band gap of the prepared heterostructures follows the trend: ZnO-NiO (3.1 eV) > ZnO-In_2O_3 (2.71 eV) > ZnO-Co_3O_4 (2.64 eV) > ZnO-MnO_2 (2.19 eV). The photocatalytic activity was influenced by the electronic structure and the band gap of heterostructure rather than its surface area. The photocatalytic activity follows the order: Co_3O_4-ZnO > In_2O_3-ZnO > ZnO-MnO_2 > ZnO-NiO. The low charge separation efficiency of ZnO-MnO_2 and its inappropriate CB edge position are the reasons for lower photocatalytic activity than Co_3O_4-ZnO and ZnO-In_2O_3 with higher band gaps.

Acknowledgements

Authors wish to acknowledge the financial support and the laboratory facilities to carry out this work under UGC-UPE project, Govt. of India. FE-SEM work was carried out at Mangalore University, India.

Conflicts of Interest

The authors declare no conflicts of interest regarding the publication of this paper.

References

[1] Wang, H.L., Zhang, L.S., Chen, Z.G., Hu, J.Q., Li, S.J., Wang, Z.H., *et al*. (2014) Semiconductor Heterojunction Photocatalysts: Design, Construction, and Photocatalytic Performances. *Chemical Society Reviews*, **43**, 5234-5244.

[2] Pirhashemi, M., AHabibi-Yangjeh, A. and Rahim Pouran, S. (2018) Review on the Criteria Anticipated for the Fabrication of Highly Efficient ZnO-Based Visible-Light-Driven Photocatalysts. *Journal of Industrial and Engineering Chemistry*, **62**, 1-25.

[3] Gnanaprakasam, A., Sivakumar, V.M., Sivayogavalli, P.L. and Thirumarimurugan, M. (2015) Characterization of TiO_2 and ZnO Nanoparticles and Their Applications in Photocatalytic Degradation of Azodyes. *Ecotoxicology and Environmental Safety*, **121**, 121-125. https://doi.org/10.1016/j.ecoenv.2015.04.043

[4] Wang, C, Xu, B.Q., Wang, X.M. and Zhao, J.C. (2005) Preparation and Photocatalytic Activity of ZnO/TiO_2 /SnO_2 Mixture. *Journal of Solid State Chemistry*, **178**, 3500-3506. https://doi.org/10.1016/j.jssc.2005.09.005

[5] Ye, Z., Li, J., Zhou, M., Wang, H., Ma, Y. and Huo, P. (2016) The Histone H3.3K36M Mutation Reprograms the Epigenome of Chondroblastomas. *Chemical Engineering Journal*, **352**, 1344-1348.

[6] Wang, J., Wang, Z., Huang, B., Ma, Y., Liu, Y., Qin, X., Zhang, X. and Dai, Y. (2012) Facile Incorporation of Aggregation-Induced Emission Materials into Mesoporous Silica Nanoparticles for Intracellular Imaging and Cancer Therapy. *ACS Applied Materials &Interfaces*, **5**, 1943-1947.

[7] Ullatil, S.G., Periyat, P., Naufal, B. and Lazar, M.A. (2016) Self-Doped ZnOMicrorods—High Temperature Stable Oxygen Deficient Platforms for Solar Photocatalysis. *Industrial & Engineering Chemistry Research*, **55**, 6413-6421. https://doi.org/10.1021/acs.iecr.6b01030

[8] Pasang, T., Namratha, K., Parvin, T., Ranganathaiah, C. and Byrappa, K. (2015) Tuning of Band Gap in TiO_2 and ZnO Nanoparticles by Selective Doping for Photocatalytic Applications. *Materials Research Innovations*, **19**, 73-80. https://doi.org/10.1179/1433075X14Y.0000000217

[9] Namratha, K., Byrappa, S. and Byrappa, K. (2013) Hydrothermal Synthesis, *in Situ* Surface Modification and Antioxidant Activity of Couple Doped Advanced ZnO Nanoparticles. *Journal of Nanopharmaceutics and Drug Delivery*, **1**, 258-265. https://doi.org/10.1166/jnd.2013.1026

[10] Chao, X., Cao, L.X., Su, G., Liu, W., Liu, H., Yu, Y.Q. and Qu, X.F. (2010) Preparationof ZnO/Cu_2O, Compound Photocatalyst and Application in Treating Organic Dyes. *Journal of Hazardous Materials*, **76**, 807-813.

[11] Hezam, A., Namratha, K., Drmosh, Q.A., Yamani, Z.H. and Byrappa, K. (2017)

Synthesis of Heterostructured Bi_2O_3-CeO_2-ZnO Photocatalyst with Enhanced Sunlight Photocatalytic Activity. *Ceramics International*, **43**, 5292-5230. https://doi.org/10.1016/j.ceramint.2017.01.059

[12] Haleem, Y.A., He, Q., Liu, D., Wang, C., Xu, W., Gan, W., *et al.* (2017) Facile Synthesis of Mesoporous Detonation Nanodiamond-Modified Layers of Graphitic Carbon Nitride as Photocatalysts for the Hydrogen Evolution Reaction. *RSC Advances*, **7**, 15390-15396.

[13] Mondal, K. and Sharma, A. (2016) Recent Advances in Synthesis and Application of Photocatalytic Metal-Metal Oxide Core-Shell Nanoparticles for Environmental Remediation and Their Recycling Process. *RSC Advances*, **6**, 83589-83612. https://doi.org/10.1039/C6RA18102C

[14] Li, J.Z., Zhong, J.B., He, X.Y., Huang, S.T., Zeng, J., He, J.J., *et al.* (2013) Enhanced Photocatalytic Activity of Fe_2O_3 Decorated Bi_2O_3. *Applied Surface Science*, **284**, 527-532. https://doi.org/10.1016/j.apsusc.2013.07.128

[15] Namratha, K. and Byrappa, K. (2013) Hydrothermal Processing and *in Situ* Surface Modification of Metal Oxide Nanomaterials. *The Journal of Supercritical Fluids*, **79**, 251-260. https://doi.org/10.1016/j.supflu.2013.01.007

[16] Namratha, K and Byrappa, K. (2012) Novel Solution Routes of Synthesis of Metal Oxide and Hybrid Metal Oxide Nanocrystals. *Progress in Crystal Growth and Characterization of Materials*, **58**, 14-42. https://doi.org/10.1016/j.pcrysgrow.2011.10.005

[17] Keerthana, D.S., Namratha, K., Byrappa, K. and Yathirajan, H.S. (2015) Facile One-Step Fabrication of Magnetite Particles under Mild Hydrothermal Conditions. *Journal of Magnetism and Magnetic Materials*, **378**, 551-557. https://doi.org/10.1016/j.jmmm.2014.10.176

[18] Shubha, P., Namratha, K., Jit Chatterjee, M.S., Mustak, B. and Byrappa, K. (2017) Use of Honey in Stabilization of ZnO Nanoparticles Synthesized via Hydrothermal Route and Assessment of Their Antibacterial Activity and Cytotoxicity. *Global Journal of Nanomedicine*, **2**, Article ID: 555585.

[19] Hezam, A., Namratha, K., Drmosh, Q., Chandrashekar, B.N., Sadasivuni, K.K., Yamaniet, Z.H., *et al.* (2017) Heterogeneous Growth Mechanism of ZnO Nanostructures and the Effects of Their Morphology on Optical and Photocatalytic Properties. *CrystEngComm*, **19**, 3299-3312. https://doi.org/10.1039/C7CE00609H

[20] Liang, Z., Jing, X., Liu, J., Wang, J. and Sun, Y. (2015) Facile Synthesis of Mesoporous ZnO/Co_3O_4 Microspheres with Enhanced Gas-Sensing for Ethanol. *Sensors and Actuators B: Chemical*, **221**, 1492-1498. https://doi.org/10.1016/j.snb.2015.07.113

[21] Huang, M., Li, F., Li, X., Luo, D., Qiu, X., Zhang, Y. and Li, G. (2015) MnO_2-Based Nanostructures for High-Performance Supercapacitors. *Electrochimica Acta*, **152**, 172-177. https://doi.org/10.1016/j.electacta.2014.11.127

[22] Radhamani, A.V., Shareef, K.M. and Ramachandra, M.S. (2016) ZnO@MnO_2 Core-Shell Nanofiber Cathodes for High Performance Asymmetric Supercapacitors. *ACS Applied Materials & Interfaces*, **8**, 30531-30542. https://doi.org/10.1021/acsami.6b08082

[23] Wang, Z., Huang, B., Dai, Y., Qin, X., Zhang, X., Wang, P., Liu, H. and Yu, J. (2009) HOx Radical Regeneration in the Oxidation of Isoprene. *Physical Chemistry Chemical Physics*, **11**, 5935-5939. https://doi.org/10.1039/b908511d

[24] Tauc, J., Grigorovici, R. and Vancu, A. (1966) Optical Properties and Electronic Structure of Amorphous Germanium. *Physica Status Solidi*, **15**, 627-637. https://doi.org/10.1002/pssb.19660150224

[25] Srivastava, M., Das, A.K., Khanra, P., Uddin, M.E., Kim, N.H. and Lee, J.H. (2013) Characterizations of *in Situ* Grown ceria Nanoparticles on Reduced Graphene Oxide as a Catalyst for the Electrooxidation of Hydrazine. *Journal of Materials Chemistry A*, **7**, 5069-5089. https://doi.org/10.1039/c3ta11311f

[26] Sing, K.S.W., Everett, D.H., Haul, R., Moscou, L., Pierotti, R.S., Rouquerol, J., *et al*. (1985) Reporting Physisorption Data for Gas/Solid Systems with Special Reference to the Determination of Surface Area and Porosity. *Pure and Applied Chemistry*, **57**, 603-619. https://doi.org/10.1351/pac198557040603

[27] Dong, F., Zhao, Z., Xiong, T., Ni, Z., Zhang, W., Sun, Y., *et al*. (2013) Metal-Free Graphitic Carbon Nitride Photocatalyst Goes into Two-Dimensional Time. *ACS Applied Materials & Interfaces*, **5**, 11392-11401. https://doi.org/10.1021/am403653a

[28] Kumar, K., Amanchi, S.R., Sreedhar, B., Ghosal, P. and Subrahmanyam, C. (2017) Phenol and Cr(VI) Degradation with Mn Ion Doped ZnO under Visible Light Photocatalysis. *RSC Advances*, **7**, 43030-43039. https://doi.org/10.1039/C7RA08172C

[29] Muñoz-Batista, M.J., Gómez-Cerezo, M.N., Kubacka, A., Tudela, D. and Fernández-García, M. (2014) Role of Interface Contact in CeO_2-TiO_2 Photocatalytic Composite Materials. *ACS Catalysis*, **4**, 63-72. https://doi.org/10.1021/cs400878b

[30] Ke, J., Liu, J., Sun, H., Zhang, H., Duan, X., Liang, P., *et al*. (2017) Facile Assembly of $Bi_2O_3/Bi_2S_3/MoS_2$ *N*-Pheterojunction with Layered *N*-Bi_2O_3 and *P*-MoS_2 for Enhanced Photocatalytic Water Oxidation and Pollutant Degradation. *Applied Catalysis B*: *Environmental*, **200**, 47-55. https://doi.org/10.1016/j.apcatb.2016.06.071

[31] Hezam, A., Namratha, K., Lakshmeesha, T.R. and Byrappa, K. (2018) Direct Z-Scheme Cs_2O-Bi_2O_3-ZnO Heterostructures as Efficient Sunlight-Driven Photocatalysts. *ACS Omega*, **3**, 12260-12269. https://doi.org/10.1021/acsomega.8b01449

[32] Marschall, R. (2014) Semiconductor Composites: Strategies for Enhancing Charge Carrier Separation to Improve Photocatalytic Activity. *Advanced Functional Materials*, **24**, 2421-2440. https://doi.org/10.1002/adfm.201303214